



Cite this: *Phys. Chem. Chem. Phys.*,
2016, 18, 12847

Overcoming artificial broadening in Gd^{3+} – Gd^{3+} distance distributions arising from dipolar pseudo-secular terms in DEER experiments†

Marie Ramirez Cohen,^a Veronica Frydman,^b Petr Milko,^b Mark A. Iron,^b
Elwy H. Abdelkader,^c Michael D. Lee,^d James D. Swarbrick,^d Arnold Raitsimring,^e
Gottfried Otting,^c Bim Graham,^d Akiva Feintuch*^a and Daniella Goldfarb*^a

By providing accurate distance measurements between spin labels site-specifically attached to bio-macromolecules, double electron–electron resonance (DEER) spectroscopy provides a unique tool to probe the structural and conformational changes in these molecules. Gd^{3+} -tags present an important family of spin-labels for such purposes, as they feature high chemical stability and high sensitivity in high-field DEER measurements. The high sensitivity of the Gd^{3+} ion is associated with its high spin ($S = 7/2$) and small zero field splitting (ZFS), resulting in a narrow spectral width of its central transition at high fields. However, under the conditions of short distances and exceptionally small ZFS, the weak coupling approximation, which is essential for straightforward DEER data analysis, becomes invalid and the pseudo-secular terms of the dipolar Hamiltonian can no longer be ignored. This work further explores the effects of pseudo-secular terms on Gd^{3+} – Gd^{3+} DEER measurements using a specifically designed ruler molecule; a rigid bis- Gd^{3+} -DOTA model compound with an expected Gd^{3+} – Gd^{3+} distance of 2.35 nm and a very narrow central transition at the W-band (95 GHz). We show that the DEER dipolar modulations are damped under the standard W-band DEER measurement conditions with a frequency separation, $\Delta\nu$, of 100 MHz between the pump and observe pulses. Consequently, the DEER spectrum deviates considerably from the expected Pake pattern. We show that the Pake pattern and the associated dipolar modulations can be restored with the aid of a dual mode cavity by increasing $\Delta\nu$ from 100 MHz to 1.09 GHz, allowing for a straightforward measurement of a Gd^{3+} – Gd^{3+} distance of 2.35 nm. The increase in $\Delta\nu$ increases the contribution of the $|-5/2\rangle \rightarrow |-3/2\rangle$ and $|-7/2\rangle \rightarrow |-5/2\rangle$ transitions to the signal at the expense of the $|-3/2\rangle \rightarrow |-1/2\rangle$ transition, thus minimizing the effect of dipolar pseudo-secular terms and restoring the validity of the weak coupling approximation. We apply this approach to the A93C/N140C mutant of T4 lysozyme labeled with two different Gd^{3+} tags that have narrow central transitions and show that even for a distance of 4 nm there is still a significant (about two-fold) broadening that is removed by increasing $\Delta\nu$ to 636 MHz and 898 MHz.

Received 5th February 2016,
Accepted 5th April 2016

DOI: 10.1039/c6cp00829a

www.rsc.org/pccp

^a Department of Chemical Physics, Weizmann Institute of Science, Rehovot 7610001, Israel. E-mail: Daniella.Goldfarb@weizmann.ac.il, Akiva.Feintuch@Weizmann.ac.il

^b Department of Chemical Research Support, Weizmann Institute of Science, Rehovot 7610001, Israel

^c Research School of Chemistry, Australian National University, Canberra, ACT 2601, Australia

^d Monash Institute of Pharmaceutical Sciences, Monash University, Parkville, VIC 3052, Australia

^e Department of Chemistry, University of Arizona, Tucson, AZ 85721, USA

† Electronic supplementary information (ESI) available: Primary DEER data model compound 7, Ka-band DEER data, additional DFT optimization data and discussion, EPR simulations and primary DEER data for T4 lysozyme. See DOI: 10.1039/c6cp00829a

Introduction

Since their introduction in 2007,¹ Gd^{3+} tags have proven to be good alternatives to nitroxide spin labels for double electron–electron resonance (DEER)² distance measurements of biomolecules in frozen solutions at high microwave (MW) frequencies, such as W-band (95 GHz) and Q-band (35 GHz).^{1,3–18} The main motivation for their development is their high sensitivity, lack of orientation selection at high fields, which allows simple data analysis and straightforward extraction of the distance distribution from the DEER data, and, importantly, their chemical stability in the reducing environment of the cellular cytosol, which renders them suitable for in-cell measurements.^{19–21} The analysis of DEER data for a pair of $S = 1/2$ spins, such as nitroxide spin

labels, is well-established, and different software packages are available for extracting distance distributions.^{22,23} It has been shown that DEER measurements with pairs of Gd^{3+} ions can be analyzed using the same software packages as if Gd^{3+} had a spin $S = 1/2$.¹ However, there are a few caveats that have to be taken into account when carrying out such an analysis. A recent study on a series of rigid molecular rulers with Gd^{3+} – Gd^{3+} distances in the range of 2.1–8.5 nm showed that, for distances below 3 nm, the data analysis procedure leads to artificial broadening of the distance distribution due to the underlying assumption that the electron–electron dipolar interaction can be described by the weak coupling approximation as in the case of a pair of nitroxides.¹⁴ The problem arises from ignoring the pseudo-secular terms of the dipolar Hamiltonian,^{5,14} as briefly summarized below.

The spin Hamiltonian of a pair of Gd^{3+} ions is given by

$$\hat{H} = \sum_{i=1,2} (\omega_{e,i} \hat{S}_{z,i} + \hat{S}_i \cdot \mathbf{D}^i \cdot \hat{S}_i) + \hat{S}_1 \cdot \mathbf{T} \cdot \hat{S}_2 \quad (1)$$

where $\omega_{e,i}$ is the Larmor frequency, \mathbf{D}^i is the zero field splitting (ZFS) tensor of each of the ions, and \mathbf{T} is the electron–electron dipole interaction tensor. In the principal axis of system \mathbf{D}^i , the ZFS is represented by the parameters $D_i = \frac{3}{2} D_{zz,i}$ and $E_i = \frac{1}{2} (D_{xx,i} - D_{yy,i})$. Due to the large Zeeman energy at high fields, truncation of both the ZFS and the dipolar parts of the Hamiltonian is justified. As we are working at a relatively high field and the ZFS of the Gd^{3+} complex is, in general, small (usually below 40 mT),²⁴ only the first order terms of the ZFS are considered for all transitions, while a second order contribution is added for the $|-1/2\rangle \rightarrow |1/2\rangle$ transition.¹⁴

For the dipolar interaction only the secular and pseudo-secular terms need to be taken into account. They are given by

$$\hat{H}_d^{\text{secular}} = \omega_{\text{dip}} \hat{S}_z^1 \hat{S}_z^2 (3 \cos^2 \theta_d - 1) \quad (2)$$

$$\hat{H}_d^{\text{pseudo-secular}} = -\frac{\omega_{\text{dip}}}{4} (\hat{S}_+^1 \hat{S}_-^2 + \hat{S}_-^1 \hat{S}_+^2) (3 \cos^2 \theta_d - 1)$$

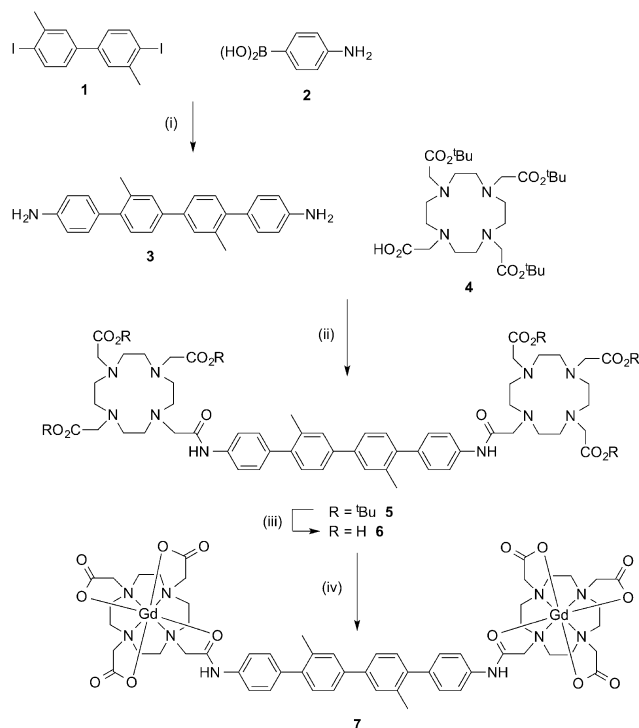
where $\omega_{\text{dip}} = \frac{\mu_B^2 g_1 g_2}{\hbar} \frac{1}{r_{12}^3}$ is the dipolar coupling frequency for an electron–electron distance of r_{12} and θ_d is the angle between the principal axis of the dipolar interaction defined by the vector connecting the two Gd^{3+} ions and the external magnetic field. Usually, DEER experiments are carried out under conditions of weak coupling, that is, when the frequency separation between the resonances of the two coupled spins, $\Delta\omega = |\omega_{e,1} - \omega_{e,2}|$, is larger than dipolar splitting, ω_{dip} . When carrying out DEER measurements on nitroxides, $\Delta\nu = \Delta\omega/2\pi$ is determined by the difference between the pump and observe pulse and is usually set to 65 MHz. For pairs separated by ~ 2 nm, $\omega_{\text{dip}}/2\pi$ is about 6.5 MHz, which is an order of magnitude less than $\Delta\nu$ and the weak coupling approximation holds.²⁵

Under typical Gd^{3+} – Gd^{3+} DEER conditions, the pump pulse is positioned at the peak of the Gd^{3+} spectrum, which predominantly arises from the central $|-1/2\rangle \rightarrow |1/2\rangle$ transition, and the detection pulses are positioned 90–100 MHz away, such that the main

contribution to the detected signal is from the $|-3/2\rangle \rightarrow |-1/2\rangle$ transition. It has been shown that, under these conditions, the Pake pattern obtained from the Fourier transform (FT) of the DEER trace is distorted for short distances (2–3 nm).^{1,14} Simulations indicate that the distortions are a result of contributions from the pseudo-secular terms of the dipolar Hamiltonian (see eqn (2)).^{3,14,26} The central transitions of the two dipolar interacting spins are separated due to differences in the D value (because of the large distribution of D values) or different orientations with respect to the magnetic field, resulting in different contributions of the second order ZFS. When this separation is small, the weak coupling approximation no longer applies and the pseudo-secular terms lead to a shift of the $|-1/2\rangle$ and $|1/2\rangle$ levels of the two spins. The contributions of the pseudo-secular terms were addressed for the case of a $S = 1/2$ pair. Under strong coupling conditions, it has been shown analytically that for the spin 1/2 case the Pake pattern is broadened by a factor of 3/2.^{27,28} As this factor depends on the spin of the system, it will be larger for a pair of 7/2 spins, and therefore, changing the requirements for meeting the weak-coupling approximation, namely a larger $\Delta\omega$ would be required. This was addressed in the ESI of ref. 5. However, this approach does not take into account the ZFS interaction explicitly, as described in our recent publication, where we showed that the weak coupling condition is more easily met when the ZFS is large.¹⁴ In this work we have performed numerical calculations that take into account the high spin as well as the fact that part of the dipolar coupled pairs are not weakly or strongly coupled but in an intermediate condition depending on their D value and orientation with respect to the external magnetic field.

It should be emphasized that in the case of a small ZFS the central transition of the observed spins is definitely not detected because the detection frequency is separated from the pump frequency by at least 100 MHz. Nonetheless, observation of the $|-3/2\rangle \rightarrow |-1/2\rangle$ transition will also be affected by the overlap of the central transitions of the two spins as it shares a common level with the $|-1/2\rangle$ level. As a consequence, data analysis with the commonly used DeerAnalysis software,²³ which is based on the weak coupling approximation, yields distance distributions that are artificially broadened and include spurious peaks to fit the distorted Pake pattern. The theory also predicts that these undesirable effects increase with decreasing distance and D value and will not be significant when detecting higher m_s transitions.

In this work, we further explore the effects of the pseudo-secular terms on Gd^{3+} – Gd^{3+} DEER using a specifically designed ruler molecule and propose experimental approaches to minimize their contributions and thus avoid artificial broadening. This is particularly important for Gd^{3+} spin labels with a small ZFS and, consequently, a narrow central transition. Notably, such spin labels are very attractive for DEER measurements because of their high EPR sensitivity. For example, compound 7 (Scheme 1) is a rigid bis- Gd^{3+} –DOTA model with a Gd^{3+} – Gd^{3+} distance of 2.35 nm and a very narrow EPR central transition (~ 1.6 mT). We show that, using the standard DEER measurement conditions with $\Delta\nu = 100$ MHz,



Scheme 1 Synthesis procedure for the bis- Gd^{3+} model compound **7**. *Reagents and conditions:* (i) $\text{Pd}(\text{PPh}_3)_4$, K_2CO_3 , toluene, H_2O , EtOH, reflux, 24 h, 60%; (ii) HOBt, DCC, DIPEA, CH_2Cl_2 , room temperature, 72 h, 75%; (iii) trifluoroacetic acid, DCM, room temperature, overnight; (iv) $\text{GdCl}_3 \cdot (\text{H}_2\text{O})_6$, NaHCO_3 , H_2O , pH 7, room temperature, 48 h, 62% (from **5**).

DEER modulations are damped and the Pake pattern is highly distorted, much more than that observed earlier for a PyMTA chelate with a Gd^{3+} – Gd^{3+} distance of 2.1 nm but with a larger ZFS.¹⁴ With the aid of a dual mode cavity, we also show that by increasing the frequency separation, $\Delta\nu$, of the detection frequency from the central transition from 100 MHz to 1.09 GHz, the distortions are reduced, the Pake pattern is recovered, and the distance of 2.35 nm is clearly obtained. The increase in $\Delta\nu$ results in an increase in the contribution of the $|-5/2\rangle \rightarrow |-3/2\rangle$ and $|-7/2\rangle \rightarrow |-5/2\rangle$ transitions to the signal at the expense of the $|-3/2\rangle \rightarrow |-1/2\rangle$ transition. The results show a gradual recovery of the non-distorted Pake pattern with an increasing shift of the detection frequency, confirming the origin of the distortions. Finally, we demonstrate this approach on the A93C/N140C mutant of T4 lysozyme labeled with two different Gd^{3+} tags that have D values of 450 and 800 MHz and show that for a distance of 4 nm there is still a significant (about two-fold) broadening under standard conditions, which is removed by increasing $\Delta\nu$ to 636 or 898 MHz, respectively.

Experimental

Spectroscopic details

The dual mode cavity. The dual mode cavity was built according to the design of Tkach *et al.*,²⁹ adapted to the different configurations of our magnet, which has a vertical bore as opposed to the horizontal bore of the magnet used by Tkach *et al.*²⁹

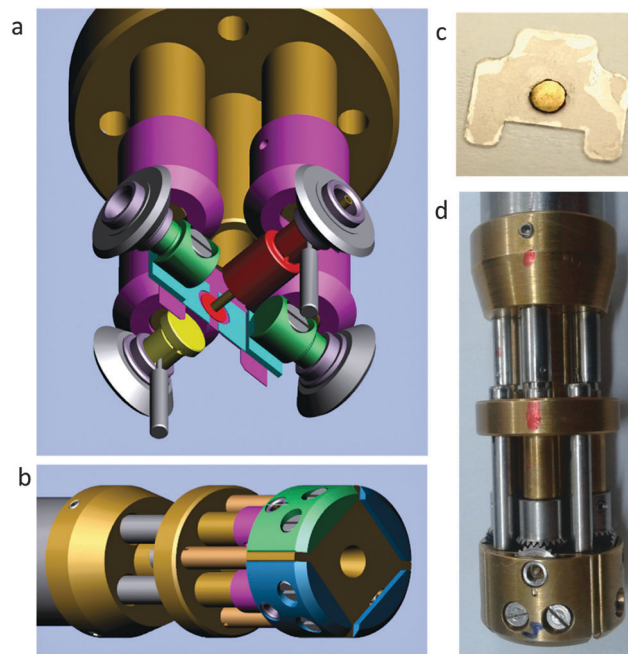


Fig. 1 (a) Internal design of the resonator and the probe head, not including the cavity itself that is aligned with the red front and yellow back pistons. The sample capillary is inserted into the red piston. The green screws hold the brass lateral slabs (shown in cyan), which change the frequency difference between the modes according to the disk diameter. (b) Coupling hole between the cavity and the waveguide. (c) Photograph of the gold-plated disk on a mica plate, which is placed in the middle of the cavity and creates the dual mode. (d) Photograph of the resonator attached to the probe.

The resonator consists of a cylindrical cavity with an inner diameter of 4.2 mm divided into two sections by a gold-plated disk on a mica plate and by two lateral gold plated brass slabs. The slabs move simultaneously in the plain of the disk such that they close the open space between the disk and the sides of the resonator. This spacing allows the formation of coupled microwave (MW) modes in both portions of the cavity. Along the longitudinal axis of the resonator, there are two pistons of different sizes facing each other, one of which has an opening to introduce samples. The pistons move independently inwards and outwards within the cavity to allow for establishing the resonance conditions of the two MW modes. Finally, coupling with the corrugated waveguide connecting the resonator to the MW bridge³⁰ is done *via* a small iris at the side of the resonator. Fig. 1 shows the internal and external design of the resonator, the golden disk on the mica plate, and a photograph of the cavity.

To obtain a wide range of frequency differences between the MW modes, several gold-plated disks of different sizes were used with diameters varying from 2.7 to 3.1 mm and a uniform thickness of 0.1 mm. A maximal $\Delta\nu = 1.09$ GHz was achieved using a 2.7 mm disk. The resonator was attached to a probe head that fits into the liquid He cryostat of our home-made W-band spectrometer.^{30,31} Fig. 2 shows the tuning profile of the MW modes of the dual cavity. The frequency difference between the modes is determined by the size of the disk and the position of the lateral slabs in the cavity. A disk of 3.1 mm diameter was

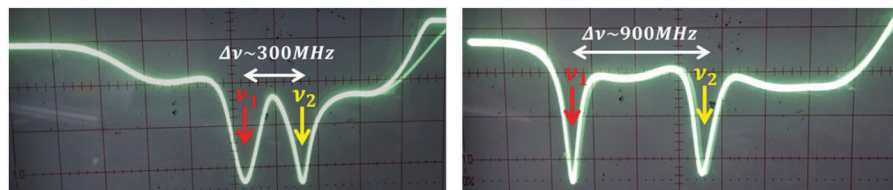


Fig. 2 Photograph of the reflected MW power vs. MW frequency of the source. The arrows show the frequencies of the MW reflection minima in the dual cavity for two disc sizes. In the DEER experiment, the positions of the pump and observe frequencies are both placed at the minima of the reflection profiles, where the absorbed MW power is maximal.

used for a frequency difference of 300 MHz, whereas a 2.7 mm diameter disk had to be used for a frequency difference of 900 MHz and above.

The pulse EPR measurements. All EPR measurements were performed at the W-band at 10 K on a home-built spectrometer.^{30,31} The echo-detected EPR (ED-EPR) spectrum was recorded using the pulse sequence $\pi/2 \rightarrow \tau \rightarrow \pi \rightarrow \tau \rightarrow \text{echo}$ while sweeping the magnetic field from 3300 to 3510 mT. The pulse lengths were 20 ns for the $\pi/2$ pulse and 40 ns for the π pulse, optimized at the frequency (94.83 GHz) and the magnetic field corresponding the maximum of the EPR spectrum (3405.4 mT); the duration of τ was 800 ns.

The DEER experiments were performed using the four-pulse sequence $\pi/2 \rightarrow \tau \rightarrow \pi \rightarrow \tau + \tau_1 \rightarrow \pi \rightarrow \tau_1 \rightarrow \text{echo}$ at the observe frequency and a π pulse at the pump frequency, which was applied at time t after the first π pulse.³² The echo intensity was measured as a function of t , which ranged from -225 ns to $\tau_1 - 500$ ns with $t = 0$ coinciding with the time τ after the first observe π pulse. In all experiments, the pump frequency was set at the maximum of the Gd^{3+} ED-EPR spectrum, while that of the observe pulses were set at a higher frequency *i.e.* on the low field side of the spectrum. For the bis- Gd^{3+} -DOTA model (compound 7 of Scheme 1), an additional DEER measurement was performed at the Ka-band using a specially designed dielectric cavity (see the ESI† for experimental details). The experimental parameters for each DEER experiment on the model compound are summarized in Table 1. Table 2 lists the parameters of the DEER experiment for the A93C/N140C mutants of T4 lysozyme labeled with C1- Gd^{3+} and C9- Gd^{3+} tags (Fig. 3) for the dual cavity as well as for a single mode cavity setup. Because of the limited bandwidth of the 95 GHz spectrometer, the low-frequency dip was set to 94.4 MHz and the field was adjusted to position the maximum of the EPR signal at this frequency. This frequency was used for the pump pulse. The

Table 1 Experimental parameters used in the DEER experiments on compound 7^a

$\Delta\nu$ (MHz)	Observe $\pi/2$ (ns)	Observe π (ns)	Pump π (ns)	τ (ns)	τ_1 (μ s)	Repetition time (ms)
106	15	30	25	550	2	1
363	17.5	35	30	450	2	1
469	17.5	35	25	550	2	1
747	20	40	35	550	2	1
1090	15	30	25	550	2	1

^a Measurement times were between 4 and 10 h.

Table 2 Experimental parameters used in the DEER experiments on T4 lysozyme^a

Tag	$\Delta\nu$ (MHz)	Observe $\pi/2$ (ns)	Observe π (ns)	Pump π (ns)	τ (ns)	τ_1 (μ s)	Repetition time (ms)
C1	636	15	30	35	450	4	1
C9	878	15	30	35	450	4	1
C1 ^b	100	15	30	15	375	4.5	0.8
C9 ^b	100	15	30	15	375	4.5	0.8

^a Measurement times were between 2.5 and 9 h. ^b Measured with a single-mode cavity.

second dip at the higher frequency was used for the observe pulses.

Materials and synthesis

General. 4,4'-Diiodo-3,3'-dimethylbiphenyl (1) was purchased from TCI Europe, 4-aminophenylboronic acid (2) was purchased from ACC Corporation and (4,7,10-tris-*tert*-butoxycarbonylmethyl-1,4,7,10-tetraazacyclododec-1-yl)-acetic acid (4) was purchased from CheMatech. Column chromatography was performed on Silica gel 60 (0.040–0.063 mm). NMR spectra were recorded on a Bruker AMX-400 NMR spectrometer. ESI MS spectrometry was performed by the Department of Chemical Research Support at the Weizmann Institute of Science.

2',3''-Dimethyl-4,4'''-diamine-*p*-quaterphenyl (3). Diiodo compound 1 (0.25 g, 0.58 mmol) and boronic acid 2 (0.25 g, 1.44 mmol) were dissolved in anhydrous toluene (12 mL) and the solution was deaerated by bubbling a stream of N_2 for 15 min. To this solution, a solution of K_2CO_3 (0.517 g, 3.74 mmol) in water (2.5 mL) was added, followed by ethanol (5 mL). N_2 bubbling was continued for 15 min and then $\text{Pd}^{(0)}(\text{PPh}_3)_4$ (67 mg, 0.058 mmol) was added. The mixture was stirred at reflux under N_2 for 24 h. The mixture was then cooled to room temperature and diluted with saturated aq. NH_4Cl (14 mL) and CH_2Cl_2 (14 mL). The organic phase was separated and the aqueous phase was extracted with CH_2Cl_2 (2×14 mL). The organic extracts were combined and washed with water (14 mL) followed by saturated NaHCO_3 (14 mL). The organic phase was dried over MgSO_4 and evaporated, leaving a solid that was purified by column chromatography using CHCl_3 as the eluent, affording compound 3 as a yellow solid (127 mg, 60%). ^1H NMR (CDCl_3) δ 2.41 (s, 6H), 3.58 (s, 4H), 6.79 (d, $J = 8$ Hz, 4H), 7.22 (d, $J = 8$ Hz, 4H), 7.33 (d, $J = 8$ Hz, 2H), 7.52 (m, 4H). MS (ESI) m/z 365 ($[\text{M} + \text{H}]^+$, 79%), 387 ($[\text{M} + \text{Na}]^+$, 78%), 403 ($[\text{M} + \text{K}]^+$, 25%), 751 ($[\text{2M} + \text{Na}]^+$, 100%), 767 ($[\text{2M} + \text{K}]^+$, 23%).

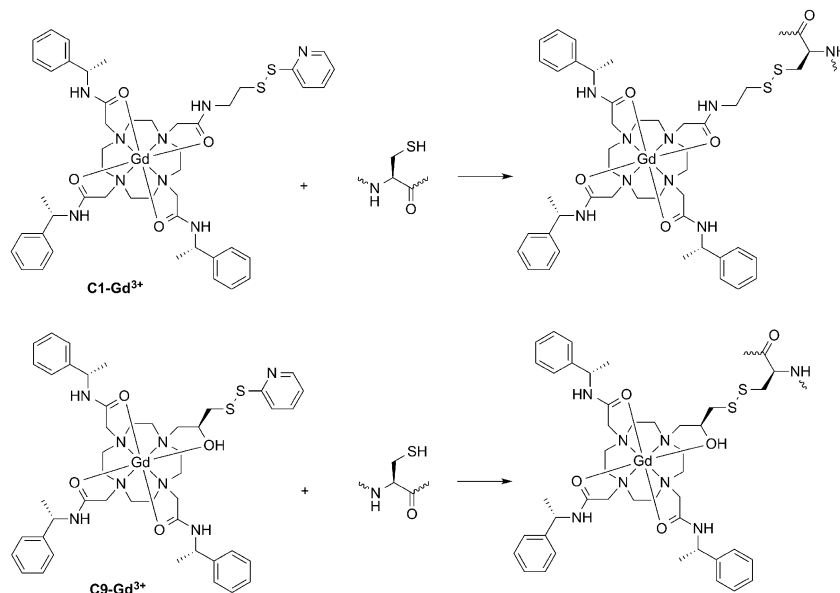


Fig. 3 Structures of the Gd^{3+} tags and the reaction scheme used to label the A93C/N140C mutant of T4 lysozyme. Each complex carries a 3+ charge (not shown).

2',3''-Dimethyl-4,4'''-bis(tris-4,7,10-*tert*-butoxycarbonylmethyl-1,4,7,10-tetraazacyclododec-1-yl-acetamidyl)-*p*-quaterphenyl (5). The DOTA derivative **4** (0.17 g, 0.297 mmol) was dissolved in anhydrous CH_2Cl_2 (3 mL) under N_2 . HOBt (1-hydroxybenzotriazole) (41 mg, 0.297 mmol) was added followed by DCC (*N,N'*-dicyclohexylcarbodiimide) (153 mg, 0.743 mmol). The mixture was stirred under N_2 for 30 min at room temperature. A solution of diamine **3** (30 mg, 0.082 mmol) in anhydrous CH_2Cl_2 (2 mL) was added, followed by DIPEA (*N,N*-diisopropylethylamine) (70 μL , 0.39 mmol). The mixture was flushed with N_2 , sealed, and stirred at room temperature for 3 days. After this time the white precipitate was filtered off and the filtrate was diluted with CH_2Cl_2 (10 mL) and washed with brine (2×3 mL), followed by 0.1 M NaOH (2×3 mL). The organic phase was washed several times with water until the pH became neutral. The organic phase was dried over Na_2SO_4 and evaporated, affording compound **5** (91 mg, 75%). MS (ESI) m/z 759 ($[\text{M} + 2\text{Na}]^{2+}$, 100%).

2',3''-Dimethyl-4,4'''-bis(tris-4,7,10-carbonylmethyl-1,4,7,10-tetraazacyclododec-1-yl-acetamidyl)-*p*-quaterphenyl (6). Compound **5** (89 mg, 0.060 mmol) was dissolved in dry CH_2Cl_2 (5 mL). TFA (trifluoroacetic acid) (5 mL) was added and the mixture was sealed and stirred overnight. The solvents were evaporated at reduced pressure and the residue was taken up in CH_3Cl and evaporated to dryness. This procedure was repeated 3 more times to eliminate any remaining TFA. The residue was dried under reduced pressure and used in its totality in the next step without any further purification.

Gd^{3+} complex of 2',3''-dimethyl-4,4'''-bis(tris-4,7,10-carbonylmethyl-1,4,7,10-tetraazacyclododec-1-yl-acetamidyl)-*p*-quaterphenyl (7). The compound from the previous step (**6**) was suspended in water (3.3 mL) and a solution of $\text{GdCl}_3 \cdot 6\text{H}_2\text{O}$ (49 mg, 0.132 mmol) in water (1.7 mL) was added. The pH of the mixture was adjusted to 7 with NaHCO_3 and the mixture was stirred for 2 days at room temperature. During that time, the pH was checked and adjusted

to 7 with NaHCO_3 several times. The solvents were then evaporated to dryness under at reduced pressure. The residue was re-suspended in water (4 mL) and acetone (40 mL) was added. The mixture was left overnight in the freezer and the precipitate was collected by centrifugation. The solid was re-dissolved in water (2 mL) and acetone (20 mL) was added. The mixture was left in the freezer for 2 h and the precipitate was collected by centrifugation. The pellet was dried under vacuum affording compound **7** as a beige solid (55 mg, 62% in two steps). MS (ESI) m/z 745 ($[\text{M} + 2\text{Na}]^{2+}$, 100%), 734 ($[\text{M} + \text{H} + \text{Na}]^{2+}$, 70%). The peaks showed the typical isotopic pattern associated with Gd complexes.

For EPR measurements, compound **7** was dissolved in 7 : 3 (v/v) D_2O /glycerol- d_8 to a final concentration of 0.05 mM. The sample was loaded into a quartz capillary with dimensions of 0.60 mm i.d. and 0.84 mm o.d. (2–3 μL sample volume).

Wild-type T4 lysozyme contains cysteine residues at positions 54 and 97. The mutant referred to in the present work as A93C/N140C contained the additional mutations C54T and C97A, which have previously been shown to not affect the structure and function of T4 lysozyme.¹⁸ Samples of T4 lysozyme A93C/N140C labeled with C1 and C9 tags (Fig. 3) were prepared as described earlier.¹⁸

Computational details

Structure optimizations were carried out using Gaussian09 Revision C.01.³³ The Pedrew–Burke–Ernzerhof (PBE) functional³⁴ including the second version of Grimme's empirical dispersion correction³⁵ was used in conjunction with the Huzinaga–Dunning double- ζ basis set³⁶ (D95) on the lighter atoms and the Stuttgart–Dresden^{37,38} (SDD) basis set-relativistic effective core potential (RECP) on lanthanum. Density fitting basis sets^{39,40} (DFBS) were generated by the automatic algorithm implemented in Gaussian09 and applied to reduce the computational cost of the calculations. The optimized structures were checked for the presence of

imaginary frequencies at the same level of theory as the geometry optimization and confirmed as local minima by the absence of imaginary frequencies. Single-point energies and rigid scans were done using the PBE0 functional^{34,41} using Orca 2.9.^{42,43} The PBE0 functional is a hybrid version of the PBE functional incorporating 25% Hartree-Fock exchange. A combination of the improved split valence (Def2-SVP) basis set⁴⁴ with smaller sets of polarization functions on light elements and the quadruple zeta valence basis set with larger sets of polarization function (Def2-QZVPP)⁴⁴ and RECP^{45,46} on lanthanum is used. The RIJCOSX approximation^{47–49} is applied to speed up the single-point energy calculations. In the RIJCOSX approximation, the two electron integrals are approximated by the RI-J approximation^{50–57} while the exchange integrals are approximated by ‘chain-of-spheres’ approximation (COSX).^{47–49} The RI-J approximation requires using an auxiliary basis set. The Ahlrichs Def2-SVP/J and Def2-QZVPP/J auxiliary basis sets for Coulomb fitting were selected on the light elements and lanthanum, respectively, as implemented in Orca. The relative energies are corrected for dispersion by the third version of the Grimme’s empirical model.⁵⁸ The NCIPLOT program, which was developed by J. Contreras-García *et al.*, was used to identify and visualize non-covalent interactions.⁵⁹ It analyzes the reduced

density gradient s of the electron density ρ $\left(s = \frac{1}{2(3\pi^2)^{1/3}} \frac{|\nabla\rho|}{\rho^{4/3}}\right)$

obtained by the single-point energy calculations at low densities. In our study, the wavefunctions obtained at the PBE0 level of theory were analyzed. The selected basis set was the standard Pople basis set of double- ζ quality with polarization functions on the main group elements (6-31G*).^{60–62} Our version of NCIPLOT was locally modified to allow for f -functions and parallelization using MPI.

Results

The bis-Gd³⁺-DOTA model, compound 7

EPR and DEER measurements. Fig. 4a shows the W-band echo-detected EPR (ED-EPR) spectrum of the bis-Gd³⁺-DOTA model compound 7 recorded at 10 K. The spectrum is similar to those of many other Gd³⁺ tags, with a sharp line (width at half height of approximately 1.6 mT) corresponding to the Gd³⁺

central transition, superimposed on a broad and rather symmetrical background due to all other transitions. The simulation of the spectrum is shown in Fig. 4b, where the contributions of the individual transitions are also displayed. The simulation was done using the EasySpin software⁶³ taking into account a distribution on D and E using the ‘DStrain’ parameter as defined in the software (FWHM of the Gaussian distribution). We found that the standard Gaussian distribution of D and E , which is often used to simulate Gd³⁺ spectra, based on a bimodal Gaussian distribution centered around D and $-D$ with a standard deviation of $|D/2|$ and with E/D varied from 0 to 1/3 with a probability $p(E/D) \propto E/D - 2(E/D)^2$, did not improve the fit.²⁴ Higher order terms could be used to improve the fit as found for example in ref. 64 and 65; however, this is beyond the scope of this work. The simulations neglected possible contributions to the linewidth due to the Gd³⁺–Gd³⁺ dipolar interaction. For this short distance and small expected ZFS, the dipolar interaction should contribute to the width of the central transition⁴ and therefore the D value obtained may be slightly overestimated.

The DEER results are shown in Fig. 5 and the primary data are shown in Fig. S1 (ESI†). In measurements the pump pulse was set to the maximum of the central transition, while the observe pulse was shifted away ($\Delta\nu$) stepwise in the range of 106 MHz to 1.09 GHz. An enlargement of the simulations presented in Fig. 4c clearly shows that the contribution of the $|-3/2\rangle \rightarrow |-1/2\rangle$ transition to the observed echo decreases with increasing $\Delta\nu$. For $\Delta\nu = 106$ MHz, the modulations are damped and the distance distribution derived from this DEER trace has a width of 2 nm centered at ~ 2.4 nm. This is in clear disagreement with the rigid structure of the molecule obtained from DFT calculations discussed below. The modulations slowly recover with increasing $\Delta\nu$, leading to narrower distance distributions. At $\Delta\nu = 1.09$ GHz, the modulations are very clear and the distance distribution shows a single major peak at a distance of 2.35 nm with a width of 0.25 nm at half-height. For $\Delta\nu = 469$ MHz, the distance distribution already gives the correct distance, but the width is still overestimated by more than two-fold. Measurements performed at the Ka-band on a dielectric cavity with $\Delta\nu = 728$ MHz also showed the expected

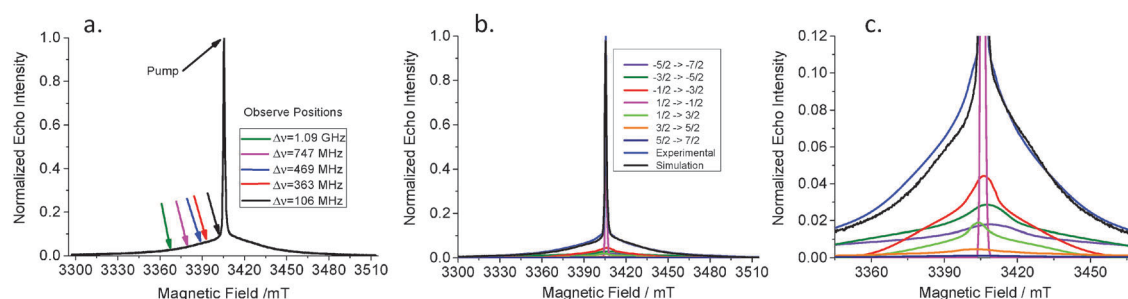


Fig. 4 W-Band ED-EPR spectrum of compound **7** at 10 K. (a) Experimental EPR spectrum. The positions of the pump pulse and the set of the observe pulses are marked. (b) CW EPR spectrum (blue line) simulated using the EasySpin software⁶³ and compared to the experimental spectrum. The individual sub-spectra of each transition are also depicted. (c) An enlargement of the simulated spectra emphasizing the field dependence of the contribution of the $|-3/2\rangle \rightarrow |-1/2\rangle$ transition (red). The parameters used in the simulation are $T = 10$ K, $D = 500$ MHz, $D\text{Strain} = 450$ MHz, $E = D/3$, $E\text{Strain} = 100$ MHz and E and D are correlated. The individual transitions are shown using the color code in the legend in (b).

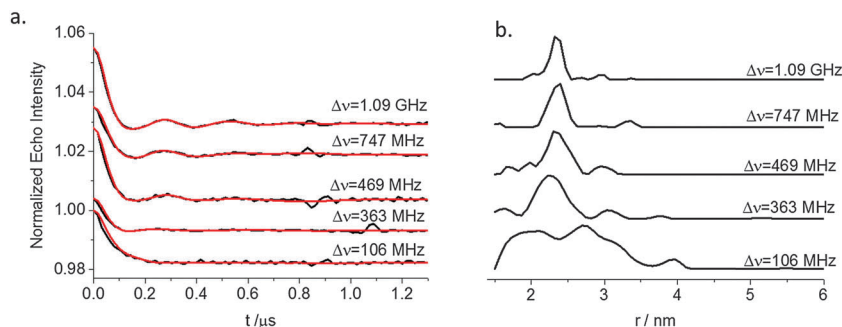


Fig. 5 W-Band DEER measurements. (a) DEER traces after background removal (black lines) with the corresponding fits obtained with DeerAnalysis²³ superimposed (red lines). The traces were all normalized to 1 and shifted in the vertical dimension for improved visual presentation. (b) Distance distributions derived by DeerAnalysis as a function of the position of the observe pulse. $\Delta\nu$ is noted for each measurement.

distance distribution (Fig. S2, ESI†). In the analysis we did not consider the possibility of the presence of an exchange interaction because we have recently shown that for Gd(III)DOTA and Gd(III)PyMTA⁶⁶ there is practically no spin density on the ligands. Moreover, the series of rulers measured recently¹⁴ showed very good agreement between the expected and the measured distance, even though the linker was highly conjugated. Finally the agreement between the measured distance and the DFT predicted distance supports this (see below).

The Fourier transforms of the DEER time domain traces are shown in Fig. 6. For $\Delta\nu = 106$ MHz the spectrum has a broad singlet with some shoulders, very different from the expected Pake pattern. As $\Delta\nu$ increases, the spectrum starts to reveal the perpendicular singularities of the Pake pattern with $\omega_{\text{dip}}/2\pi = 3.8$ MHz. At $\Delta\nu = 1.09$ GHz, the spectrum fully resembles the expected Pake pattern. All spectra show a small doublet with $\omega_{\text{dip}}/2\pi = 1.65$ MHz, which we attribute to an additional longer distance (3.2 nm) possibly due to some impurity. To reproduce the general trends of the dipolar spectra shown in Fig. 6, we used a simple model assuming that the spectra are a superposition of three contributions. One is a

Pake pattern corresponding to a distance of 2.35 nm. This contribution is expected when the pseudo-secular terms can be neglected; namely when the contributions of the higher m_s transitions $|\pm 7/2\rangle \leftrightarrow |\pm 5/2\rangle$ and $|\pm 5/2\rangle \leftrightarrow |\pm 3/2\rangle$ to the observed echo are dominant and when the larger D values within the distribution contribute to the $|\pm 3/2\rangle \leftrightarrow |\pm 1/2\rangle$ transition. The second contribution to the spectrum arises from the observation of the $|\pm 3/2\rangle \leftrightarrow |\pm 1/2\rangle$ transition, where we expect distortions due to the pseudo-secular term of the dipolar interaction. These distorted spectra were calculated by an approximation described in a previous publication¹⁴ using a Gaussian distribution for D with a mean of 500 MHz and a full width at half maximum (FWHM) of 300 MHz (neglecting the contribution of E). The third contribution is an additional Pake doublet to account for the small splitting arising from the impurity. The three spectra (with the areas of each normalized to 1) were summed with different relative contributions to reproduce the experimental spectra shown in Fig. 6. Table 3 lists the relative contributions of different components to different measurements. The calculated spectra reproduce the general trends of the experimental spectra and the fit of the individual spectra is reasonable considering the simplicity of the model. In general, the trend in Table 3 follows expectations that the contribution of the pseudo-secular dipolar interaction decreases as the detection is shifted towards higher m_s transitions. However, the contributions listed in Table 3 are not compatible with the relative contributions used for the simulation of the EPR spectrum (Fig. 4). This is because the contributions of the “distorted” spectrum depend not only on the relative contributions of the $|-3/2\rangle \rightarrow |-1/2\rangle$ and $|1/2\rangle \rightarrow |3/2\rangle$ transitions, but

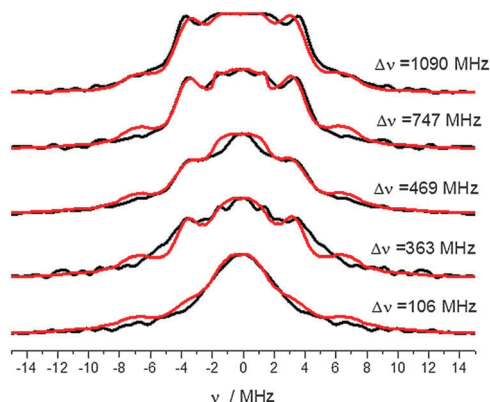


Fig. 6 Fourier transform of the experimental DEER traces shown in Fig. 5b (black trace) along with simulations in red. See the text for details on the simulations. The artifact appearing at around $t = 0.9$ μs in the time domain traces (Fig. 5 and Fig. S1, ESI†) was manually corrected (two points) prior to FT for the traces with $\Delta\nu = 363$, 469 and 747 MHz to avoid extra ripples in the baseline.

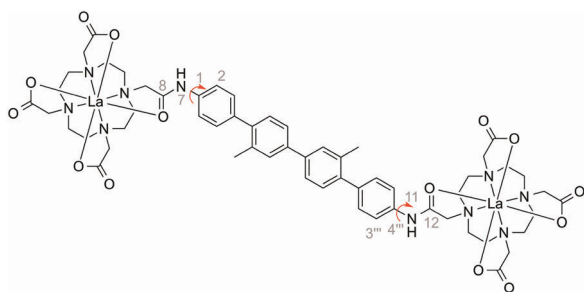
Table 3 Relative contributions of the three components discussed in the text to the calculated FT DEER spectra

Frequency	Pake pattern – $\omega_{\text{dip}}/2\pi =$ 3.8 MHz	Pake pattern – $\omega_{\text{dip}}/2\pi =$ 1.65 MHz	Calculated spectrum including pseudo-secular term
106 MHz	0.29	0.17	0.54
363 MHz	0.47	0.05	0.48
469 MHz	0.47	0.09	0.44
747 MHz	0.58	0.05	0.37
1090 MHz	0.70	0.05	0.25

also on the D value. The frequency separation between the central transitions of the observe and pumped spins, which determines the validity of the weak coupling approximation, will be bigger for larger D values. Accordingly, an increasing $\Delta\nu$ parameter not only reduces the contributions of the $|-3/2\rangle \rightarrow |-1/2\rangle$ and $|1/2\rangle \rightarrow |3/2\rangle$ transitions, but also increases the relative contributions of spins with a large D value. Therefore the effect of the pseudo-secular terms diminishes further, thus effectively reducing the contributions of the pseudo-secular terms associated with the $|-3/2\rangle \rightarrow |-1/2\rangle$ and $|1/2\rangle \rightarrow |3/2\rangle$ transitions. The contributions of the impurities are expected to be constant and independent of $\Delta\nu$, but for $\Delta\nu = 106$ and 469 MHz they are larger than the other three. We attribute this to experimental error but cannot exclude contributions from simplifications in the simulations that are manifested in the low $\Delta\nu$ values.

This series thus shows that, for $\Delta\nu = 106$ MHz, which is the commonly used value for standard single-mode cavities, and a very narrow central EPR line ($D = 500$ MHz), the effects of the pseudo-secular terms are considerably larger than those for previously reported Gd–PyMTA complexes, for which $D = 1150$ MHz. If one, therefore, uses a Gd³⁺ tag based on DOTA to improve sensitivity, it is advisable to set the observe pulse at least to 500 MHz from the pump pulse frequency in DEER measurements of short (<3 nm) distances. Because of the small D value, the signal is sufficiently large to allow such DEER measurements with a reasonable signal-to-noise ratio (SNR). These arguments equally hold for the situation where the observe frequency is set to the central transition and the pump pulse is on the other transitions.

DFT calculations. Compound 7 is not a completely rigid molecule and rotations are possible around the bonds between the amide nitrogens and the terminal phenyl rings of the spacer group (Scheme 2). An ensemble of different rotamers would broaden the width of the distance distribution. To account for this and to predict the Gd³⁺–Gd³⁺ distance distribution, we carried out DFT geometry optimizations (see Computational methods for details). To facilitate the calculations, we replaced the open shell Gd³⁺ ion by the closed shell La³⁺ and searched for the minimum energy conformer of the La³⁺ analogue of compound 7 (Scheme 2). The lanthanides are known to have similar coordination properties and the use of La³⁺ provides a tractable diamagnetic system. A relaxed scan around the C(5')–C(4')–C(1'')–C(2'') (see Scheme S1, ESI†) dihedral angle was performed



Scheme 2 The quaterphenyl-4,4'-diamine-bis DOTA–La complex. Red arrows identify freely rotatable bonds.

at the PBE/SDD level of theory for the N,N' -(2',3''-dimethyl-[1,1':4',1''4'',1'''-quaterphenyl]-4,4'''-diyl)diacetamide linker without the La³⁺ complex (Scheme S1, ESI†). The energy profile (Fig. S2, ESI†) has four maxima and four minima. The energy barriers of the rotation are low, suggesting free rotation around the C(4')–C(1'') bond. This was taken into account in the calculation of the distance distribution.

In the next step, several isomers of the DO3A–La³⁺ complex were identified (Fig. S5 and Table S1, ESI†). Generally, Ln³⁺ cations have a coordination number of eight or nine.⁶⁷ A coordination number of eight has been observed by X-ray crystallography for the DOTA–La³⁺ complex,⁶⁸ but higher coordination numbers ($n = 9, 10$) have been observed by mass spectrometry, although a complementary DFT study suggested, that the ninth and tenth ligands are located in the second solvation sphere.⁶⁹ Compound 7 offers eight coordination sites for each Ln³⁺ ion. The final model of the quaterphenyl-4,4'-diamine-bis DOTA–La³⁺ complex was built by linking two units of the most stable isomer of DO3A–La³⁺ (see Fig. S5 and Table S1, ESI†). The model was optimized and followed by rigid scans of the rotations around the C(1)–C(2)–N(7)–C(8) and C(3''')–C(4''')–N(11)–C(12) dihedral angles (red arrows in Scheme 2).

Fig. 7 shows the dependence of relative energy on the La₁⋯La₂ distance. The lowest energy belongs to a complex with a La₁⋯La₂ distance of 2.33 nm (Fig. 8), which is in excellent agreement with the experimental results. The highest calculated energy of 8.5 kcal mol^{−1} is easily accessible at room temperature, which is supported by the Boltzmann distribution of the rotational conformers (Fig. 8). The predicted distance distribution is narrow (<0.05 nm). Experimentally we observed a width of 0.25 nm when using $\Delta\nu = 1.09$ GHz.

T4 lysozyme

To estimate the extent of broadening expected in distance distributions measured in proteins, we conjugated the C1 and C9 Gd³⁺ tags (Fig. 3) to the A93C/N140C mutant of T4 lysozyme and carried out DEER measurements with the standard single-mode cavity using $\Delta\nu = 100$ MHz and with the dual-mode cavity using a very large $\Delta\nu$ (Table 2). Both tags feature a narrow EPR spectrum as shown in Fig. 9, with the C1 tag having a somewhat narrower spectrum. Simulations yield $D = 450$ MHz for the C1

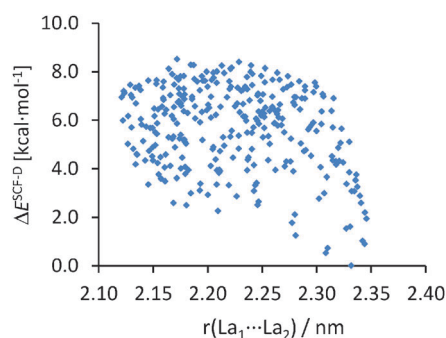


Fig. 7 Profile of conformer energies ($\Delta_{\text{rel}}E^{\text{SCF}}$) as a function of the La₁⋯La₂ distance for all structures obtained by rigid scans around the C(1)–C(2)–N(7)–C(8) and C(3''')–C(4''')–N(11)–C(12) dihedral angles of the quaterphenyl-4,4'-diamine-bis DOTA–La complex.

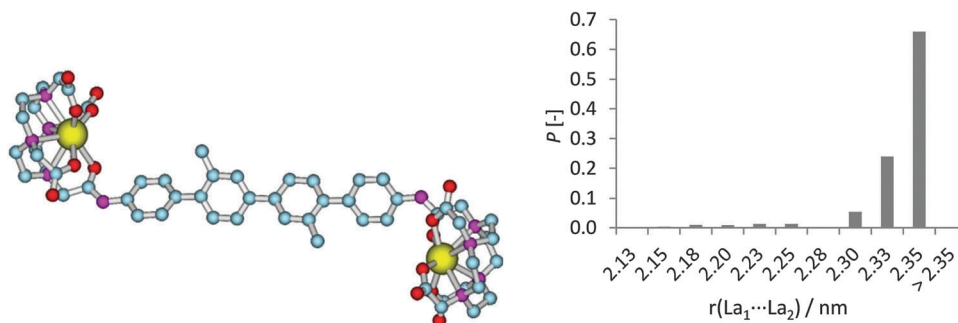


Fig. 8 Conformations of the quaterphenyl-4,4'-diamine-bis DOTA–La complex. (a) Energy-minimized structure. Color code: C: blue, N: purple, O: red, La: yellow. The hydrogen atoms are omitted for clarity. (b) Boltzmann distribution of the rotational conformers of the quaterphenyl-4,4'-diamine-bis DOTA–La complex at 298.15 K.

tag and $D = 800$ MHz for the C9 tag (Fig. S6, ESI†). The simulations used a bimodal Gaussian distribution centered about D and $-D$ with a width of $|D/2|$, and E/D was varied from 0 to $1/3$ with a probability of $p(E/D) \propto E/D - 2(E/D)^2$.²⁴

The DEER results are shown in Fig. 10. The Gd^{3+} – Gd^{3+} distances for both tags are around 4 nm. For the measurements with $\Delta\nu = 100$ MHz, the distance distributions clearly contain artificial broadening due to disregarding the pseudo-secular terms in the analysis. For the large $\Delta\nu$, the damping of the modulations is reduced and the distance distribution narrows considerably for both tags, and the maxima of the distance distribution shift slightly to longer distances. Comparison with the calculated distance distributions based on the crystal structure of T4 lysozyme and taking into account all rotamers of C1 and C9 that avoid steric clashes with the protein give very good agreement with the distance distributions derived from the DEER measurements with the large $\Delta\nu$ values.¹⁸ This indicates that the artificial broadening has been removed.

Discussion

One of the virtues of Gd^{3+} – Gd^{3+} distance measurements using DEER is the high sensitivity that can be obtained at Q- and W-band spectrometer frequencies due to the narrow width of the central transition in the EPR spectra of Gd^{3+} complexes. W-band DEER has been shown to be superior to Q-band measurements¹²

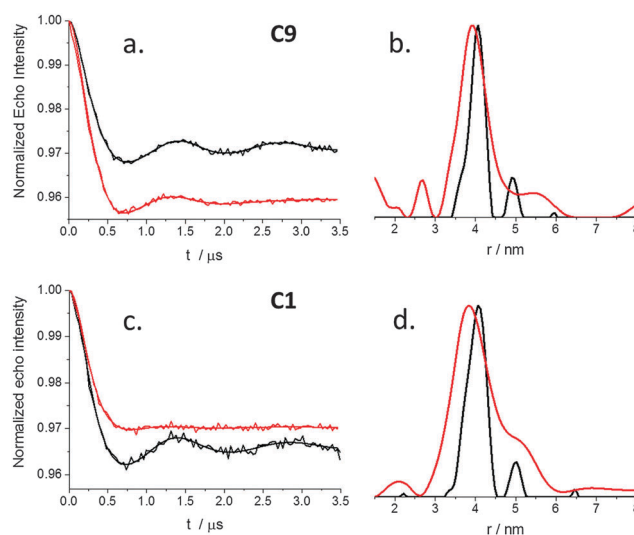


Fig. 10 W-Band DEER measurements of T4 lysozyme A93C/N140C ligated with two Gd^{3+} tags. (a) DEER traces recorded at 10 K of the sample with C9– Gd^{3+} tags after background removal using $\Delta\nu = 100$ MHz (red) or $\Delta\nu = 898$ MHz (black). The solid lines represent the fits obtained by DeerAnalysis (Tikhonov regularization) from the distance distributions shown in (b). (c and d) Same as (a and b), except using the C1– Gd^{3+} tag and $\Delta\nu = 100$ MHz (red) and $\Delta\nu = 636$ MHz (black).

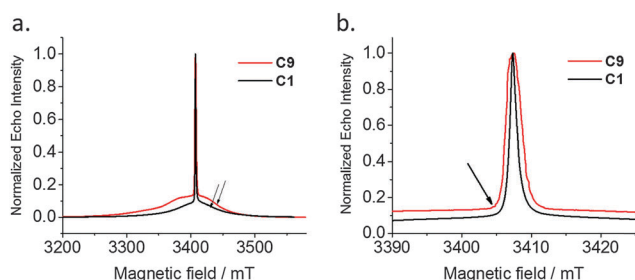


Fig. 9 W-Band ED-EPR spectrum of T4 lysozyme A93C/N140C conjugated with C1– Gd^{3+} and C9– Gd^{3+} tags. (a) Full range spectrum with arrows marking the position of the observe pulses in measurements using the dual-mode cavity. (b) Expanded spectral region with the arrow marking the position of the observe pulses in the DEER measurements using the single-mode cavity.

mainly because of the narrower central transition, which is proportional to D^2/ν_0 , where ν_0 is the spectrometer frequency. However, sensitivity is not the only factor to be considered when evaluating the efficiency of DEER measurements as the data analysis plays an important role and should be as simple as that for a pair of nitroxide spin labels at X- and Q-band frequencies. For Q-band orientation selection can be ignored under standard experimental conditions, and therefore, the extraction of the distance distribution from the DEER data is rather straightforward. At W-band, orientation selection can be neglected for Gd^{3+} – Gd^{3+} DEER measurements but not for nitroxides.^{70–73} Therefore, distance distributions are easy to extract from W-band Gd^{3+} – Gd^{3+} DEER measurements. For Gd^{3+} – Gd^{3+} DEER to become a routine tool for measurements of distance distributions, one would like to employ the same data analysis approach that is used for a pair of $S = 1/2$ spins under the weak coupling conditions using

DeerAnalysis²³ or similar software.²² However, the experimental and theoretical results show that, depending on the ZFS value and the Gd^{3+} – Gd^{3+} distance, the weak coupling approximation may not fully apply for a pair of $S = 7/2$ spins, in which case the traditional analysis results in artificial broadening of the extracted distance distribution.¹⁴ For a highly distributed D value centered at 1150 MHz, significant broadening appears for distances below 3.4 nm and the broadening increases for shorter distances. Since DEER is usually applied to biological macromolecules and the Gd^{3+} tags used so far exhibit some intrinsic flexibility, the additional broadening arising from ignoring the dipolar pseudo-secular terms in the data analysis has been assumed to be masked by the contribution from tag flexibility and internal flexibility of the system studied.^{11,15,74} This may be true for Gd^{3+} tags with relatively large ZFS (>1000 MHz). However, for Gd^{3+} tags with a small ZFS, which are particularly attractive due to the sensitivity they can impart, the contribution of the pseudo-secular terms is expected to grow and the artificial broadening cannot be overlooked. It is particularly relevant when not only the maximum of the distance distribution but also its width is to be interpreted in structural terms. For example, DEER measurements can conceivably report on protein conformational equilibria.⁷⁵ Relatively rigid tags such as the C9 tag would be best suited for such applications.¹⁸ The contribution of the pseudo-secular terms of the dipolar interaction is, in principle, also relevant for Mn^{2+} – Mn^{2+} ($S = 5/2$) distance measurements, although the effect has been found to be negligible for a peptide labeled with the maleimide DOTA– Mn^{2+} complex, which has a rather flexible tether.²⁶

In the present work, we demonstrate that the artificial broadening observed for Gd^{3+} spin labels featuring small D values in the range of 450–800 MHz is indeed significant also for a Gd^{3+} – Gd^{3+} distance of 4 nm (Fig. 10). This broadening can be avoided by choosing a sufficiently large frequency difference between the pump and observe pulses such that the contributions of the $|\pm 3/2\rangle \leftrightarrow |\pm 1/2\rangle$ transitions are minimized. We set the pump pulse to the central transition and the observe pulse to the broad background arising from the other transitions and used a dual-mode cavity to allow for large $\Delta\nu$ values. In principle, the frequencies of the observe and pump pulses can be swapped, yielding a lower modulation depth but a higher echo intensity and probably also a better SNR for the DEER trace.^{12,14} The use of a large $\Delta\nu$ value reduced the sensitivity of the experiment for two reasons. First, the quality factor (Q) of the dual cavity was not optimal; this is a technical issue and, therefore, not discussed further here. The second reason is a consequence of the echo intensity at the position of the observe frequency, which depends on D and, therefore, on the total spectral width, the temperature and the phase memory time. The latter was reported to be transition dependent, decreasing with $|m_s|$.⁷⁶ This dependence can be eliminated by observing the central transition. Increasing the temperature would lower the phase memory time⁷⁶ but increase the intensity of the central transition. Therefore, we continue to consider the optimal temperature to be around 10 K. The ED-EPR spectra shown in Fig. 9 suggest that the observed echo measured with $\Delta\nu = 900$ MHz was reduced by 43% for the

C1 tag and by 50% for the C9 tag compared to measurements using $\Delta\nu = 100$ MHz. In practice, the loss is partially compensated by the lesser echo reduction effect due to the pump pulse⁷⁷ afforded by the larger frequency separation;⁷⁸ although, we estimate the echo reduction effect in our setup to be rather small (at most 20%). In principle, the loss due to reduced EPR intensity far away from the central transition can be further compensated by optimizing the dual cavity to have a high Q at the observe dip, which would enhance the observed signal compared to measurements with a single-mode cavity, where one would place the observe pulses away from the center of the cavity resonance profile.

When a dual mode cavity or an ultra-broad bandwidth cavity^{72,79} are not available, it is advisable to use two types of Gd^{3+} tags, one for short distances and another for long distances. For the short distance range (2.5–5 nm), a tag with a large D value, like PyMTA¹⁹ or the C3-tag^{17,80} could be used. The C3-tag was developed for conjugation to the unnatural amino acid *p*-azido-phenylalanine as opposed to a cysteine residue. It produces distance distributions with maxima that can be predicted with remarkable accuracy.¹⁷ For such tags we still expect some artificial broadening for distances shorter than 3.4 nm. For distances above 5 nm the SNR is crucial and a DOTA derivative like the C1 or the C9-tag should be used. The approach of using two different tags may be more demanding in terms of sample preparation, but may be acceptable as the sample amounts needed are very small (2–3 μL or 0.05–0.1 mM protein per sample). It has been shown that the C9 tag does not exhibit any artificial broadening for a Gd^{3+} – Gd^{3+} distance of 6 nm with the usual setting of $\Delta\nu = 100$ MHz.¹⁸ This approach, similar to the use of a large $\Delta\nu$ value, will compromise the SNR due to the larger EPR linewidth of the tag used for short distances. In contrast to the C9-tag, many tags such as maleimide-DOTA and MTS-DOTA^{3,11,20} feature narrow EPR lines but are rather flexible, giving inherently broadened distance distributions, which will in any case be difficult to analyze in terms of protein and tag flexibility. In the future, it will be useful to tabulate the extent of artificial broadening expected in the distance distributions for particular Gd^{3+} – Gd^{3+} distances as a function of the D value and commonly observed D and E distributions. This can be done theoretically and such calculations are currently underway in our laboratory. The analysis of DEER traces measured with a small $\Delta\nu$ using the full spin Hamiltonian, including the ZFS and the dipolar pseudo-secular terms, would require the knowledge of D and E and their distributions and would require large computation resources.

Recently, the relaxation-induced dipolar modulation enhancement (RIDME) experiment, which also measures electron–electron dipolar interactions, has been reported to be highly effective for W-band Gd^{3+} – Gd^{3+} distance measurements because it generates greater modulation depths than DEER.⁸¹ In this experiment, potentially all spin pairs in the system contribute to the dipolar modulation and not only those affected by the pulse pump as in the DEER experiment. In this situation, the contributions from the $|\pm 3/2\rangle \leftrightarrow |\pm 1/2\rangle$ transitions should no longer be dominant and one would expect less broadening than with DEER. The caveat here is the presence of harmonics of the fundamental

dipolar frequency (and therefore multiple distances) due to the presence of multi-quantum relaxation pathways, that makes it hard to analyze broad distance distributions. Finally, the use of chirp pulses optimized for selecting transitions other than the $|\pm 3/2\rangle \leftrightarrow |\pm 1/2\rangle$ transitions may also reduce the artificial broadening.⁸²

Conclusions

Using a specifically designed bis-Gd³⁺ model compound with a small ZFS and a short Gd³⁺–Gd³⁺ distance, we have demonstrated experimentally that ignoring dipolar pseudo-secular terms in the analysis of DEER traces introduces extensive broadening in the distance distribution for a Gd³⁺–Gd³⁺ distance of 2.35 nm. These artifacts can be reduced by increasing the frequency separation between the observe and pump pulses to reduce the contributions of the $|\pm 3/2\rangle \leftrightarrow |\pm 1/2\rangle$ transitions to the observed echo. For a sufficiently large $\Delta\nu$ value, 1.09 GHz in this particular case, the undistorted dipolar Pake pattern is recovered and the true distance is extracted, as substantiated by DFT calculations. This was further demonstrated by a practical application using a double mutant of T4 lysozyme labeled with the C1 and C9 Gd³⁺-tags and a distance of about 4 nm, that exhibit narrow central transitions and *D* values in the range of 450–800 MHz.

Acknowledgements

We thank Dr Igor Tkach and Prof. Marina Bennati for their help and advice in the design of the dual cavity probe head. We also acknowledge the help of Dr Royi Kaufmann and Dr Ilia Kaminker in the initial design of the dual-mode cavity probe head. This research was supported by the Israeli Science Foundation (grant 334/14) and made possible in part by the historic generosity of the Harold Perlman Family. D. G. holds the Erich Klieger professorial chair in Chemical Physics.

References

- 1 A. M. Raitsimring, C. Gunanathan, A. Potapov, I. Efremenko, J. M. L. Martin, D. Milstein and D. Goldfarb, *J. Am. Chem. Soc.*, 2007, **129**, 14138.
- 2 A. D. Milov, K. M. Salikhov and M. Shirov, *Fiz. Tverd. Tela*, 1981, **23**, 975–982.
- 3 A. Feintuch, G. Otting and D. Goldfarb, *Methods Enzymol.*, 2015, **563**, 415–457.
- 4 D. Goldfarb, *Phys. Chem. Chem. Phys.*, 2014, **16**, 9685–9699.
- 5 A. Potapov, Y. Song, T. J. Meade, D. Goldfarb, A. V. Astashkin and A. Raitsimring, *J. Magn. Reson.*, 2010, **205**, 38–49.
- 6 A. Potapov, H. Yagi, T. Huber, S. Jergic, N. E. Dixon, G. Otting and D. Goldfarb, *J. Am. Chem. Soc.*, 2010, **132**, 9040.
- 7 Y. Song, T. J. Meade, A. V. Astashkin, E. L. Klein, J. H. Enemark and A. Raitsimring, *J. Magn. Reson.*, 2011, **210**, 59–68.
- 8 H. Yagi, D. Banerjee, B. Graham, T. Huber, D. Goldfarb and G. Otting, *J. Am. Chem. Soc.*, 2011, **133**, 10418–10421.
- 9 D. Goldfarb, in *Structure and Bonding*, ed. C. Timmel, J. Harmer, 2014, vol. 152, pp. 163–204.
- 10 M. Yulikov, P. Lueders, M. Farooq Warsi, V. Chechik and G. Jeschke, *Phys. Chem. Chem. Phys.*, 2012, **14**, 10732.
- 11 E. Matalon, T. Huber, G. Hagelueken, B. Graham, V. Frydman, A. Feintuch, G. Otting and D. Goldfarb, *Angew. Chem., Int. Ed.*, 2013, **52**, 11831–11834.
- 12 A. Raitsimring, A. V. Astashkin, J. H. Enemark, I. Kaminker, D. Goldfarb, E. D. Walter, Y. Song and T. J. Meade, *Appl. Magn. Reson.*, 2013, **44**, 649–670.
- 13 D. T. Edwards, T. Huber, S. Hussain, K. M. Stone, M. Kinnebrew, I. Kaminker, E. Matalon, M. S. Sherwin, D. Goldfarb and S. Han, *Structure*, 2014, **22**, 1677–1686.
- 14 A. Dalaloyan, M. Qi, S. Ruthstein, S. Vega, A. Godt, A. Feintuch and D. Goldfarb, *Phys. Chem. Chem. Phys.*, 2015, **17**, 18464–18476.
- 15 N. Manukovsky, V. Frydman and D. Goldfarb, *J. Phys. Chem. B*, 2015, **119**, 13732–13741.
- 16 D. Barthelmes, M. Gränz, K. Barthelmes, K. N. Allen, B. Imperiali, T. Prisner and H. Schwalbe, *J. Biomol. NMR*, 2015, 275–282.
- 17 E. H. Abdelkader, A. Feintuch, X. Yao, L. A. Adams, L. Aurelio, B. Graham, D. Goldfarb and G. Otting, *Chem. Commun.*, 2015, **51**, 15898–15901.
- 18 E. H. Abdelkader, M. D. Lee, A. Feintuch, M. Ramirez Cohen, J. D. Swarbrick, G. Otting, B. Graham and D. Goldfarb, *J. Phys. Chem. Lett.*, 2015, **6**, 5016–5021.
- 19 M. Qi, A. Groß, G. Jeschke, A. Godt and M. Drescher, *J. Am. Chem. Soc.*, 2014, **136**, 15366–15378.
- 20 A. Martorana, G. Bellapadrone, A. Feintuch, E. Di Gregorio, S. Aime and D. Goldfarb, *J. Am. Chem. Soc.*, 2014, **136**, 13458–13465.
- 21 F.-X. Theillet, A. Binolfi, B. Bekei, A. Martorana, H. M. Rose, M. Stuiiver, S. Verzini, D. Lorenz, M. van Rossum, D. Goldfarb and P. Selenko, *Nature*, 2016, 1–19.
- 22 R. A. Stein, A. H. Beth and E. J. Hustedt, *Methods Enzymol.*, 2015, **563**, 531–567.
- 23 G. Jeschke, V. Chechik, P. Ionita, a. Godt, H. Zimmermann, J. Banham, C. R. Timmel, D. Hilger and H. Jung, *Appl. Magn. Reson.*, 2006, **30**, 473–498.
- 24 A. M. Raitsimring, A. V. Astashkin, O. G. Poluektov and P. Caravan, *Appl. Magn. Reson.*, 2005, **28**, 281–295.
- 25 G. Jeschke and Y. Polyhach, *Phys. Chem. Chem. Phys.*, 2007, **9**, 1895–1910.
- 26 H. Y. Vincent Ching, P. Demay-Drouhard, H. C. Bertrand, C. Policar, L. C. Tabares and S. Un, *Phys. Chem. Chem. Phys.*, 2015, **17**, 23368–23377.
- 27 K. M. Salikhov, V. F. Yudanov, A. M. Raitsimring, G. M. Zhidomirov and Y. D. Tsvetkov, *Colloq. AMPERE XV*, Amsterdam, North-holl, 1969, pp. 278–284.
- 28 V. F. Yudanov, K. M. Salikhov, G. M. Zhidomirov and Y. D. Tsvetkov, *Teor. Eksp. Kim.*, 1969, **5**, 663–668.
- 29 I. Tkach, G. Sicoli, C. Höbartner and M. Bennati, *J. Magn. Reson.*, 2011, **209**, 341–346.
- 30 F. Mentink-Vigier, A. Collauto, A. Feintuch, I. Kaminker, V. Tarle and D. Goldfarb, *J. Magn. Reson.*, 2013, **236**, 117–125.
- 31 D. Goldfarb, Y. Lipkin, A. Potapov, Y. Gorodetsky, B. Epel, A. M. Raitsimring, M. Radoul and I. Kaminker, *J. Magn. Reson.*, 2008, **194**, 8–15.

- 32 M. Pannier, S. Veit, A. Godt, G. Jeschke and H. W. Spiess, *J. Magn. Reson.*, 2000, **142**, 331–340.
- 33 M. J. Frisch, G. W. Trucks, H. B. Schlegel, G. E. Scuseria, M. A. Robb, G. Cheeseman, J. R. Scalmani, V. Barone, B. Mennucci, G. A. Petersson, H. Nakatsuji, M. Caricato, X. Li, H. P. Hratchian, A. F. Izmaylov, J. Bloino, G. Zheng, J. L. Sonnenberg, M. Hada, M. Ehara, K. Toyota, R. Fukuda, J. Hasegawa, M. Ishida, T. Nakajima, Y. Honda, O. Kitao, H. Nakai, T. Vreven, J. E. Montgomery, Jr., J. A. Peralta, F. Ogliaro, M. Bearpark, J. J. Heyd, E. Brothers, K. N. Kudin, R. Staroverov, V. N. Kobayashi, K. Normand, J. Raghavachari, A. Rendell, J. C. Burant, S. S. Iyengar, J. Tomasi, M. Cossi, N. Rega, N. J. Millam, M. Klene, J. E. Knox, J. B. Cross, V. Bakken, C. Adamo, J. Jaramillo, R. Gomperts, R. E. Stratmann, O. Yazyev, A. J. Austin, R. Cammi, C. Pomelli, J. W. Ochterski, R. L. Martin, K. Morokuma, V. G. Zakrzewski, G. A. Voth, P. Salvador, J. J. Dannenberg, S. Dapprich, A. D. Daniels, Ö. Farkas, J. B. Foresman, J. V. Ortiz, J. Cioslowski and D. J. Fox, *Gaussian 09, Revis. C.01*, Gaussian, Inc., Wallingford CT, 2009.
- 34 J. P. Perdew, K. Burke and M. Ernzerhof, *Phys. Rev. Lett.*, 1996, **77**, 3865–3868.
- 35 S. Grimme, *J. Comput. Chem.*, 2006, **27**, 1787–1799.
- 36 T. H. Dunning and P. J. Hay, *Modern Theoretical Chemistry*, Plenum, New York, 1976.
- 37 X. Cao and M. Dolg, *J. Chem. Phys.*, 2001, **115**, 7348–7355.
- 38 X. Cao and M. Dolg, *J. Mol. Struct.: THEOCHEM*, 2002, **581**, 139–147.
- 39 B. I. Dunlap, *J. Chem. Phys.*, 1983, **78**, 3140–3142.
- 40 B. I. Dunlap, *J. Mol. Struct.: THEOCHEM*, 2000, **529**, 37–40.
- 41 C. Adamo and V. Barone, *J. Chem. Phys.*, 1999, **110**, 6158.
- 42 F. Neese, F. Wennmohs, U. Becker, D. Bykov, D. Ganyushin, A. Hansen, R. Izsak, D. G. Liakos, C. Kollmar, S. Kossmann, D. A. Pantazis, T. Petrenko, C. Reimann, C. Riplinger, M. Roemelt, B. Sandhöfer, I. Schapiro, K. Sivalingam, B. Wezislá, M. Kállay, S. Grimme and E. Valeev, *ORCA – An ab initio, DFT semiempirical SCF-MO Packag. – Version 2.9*, 2012.
- 43 F. Neese, *Wiley Interdiscip. Rev.: Comput. Mol. Sci.*, 2012, **2**, 73–78.
- 44 F. Weigend and R. Ahlrichs, *Phys. Chem. Chem. Phys.*, 2005, **7**, 3297.
- 45 M. Dolg, H. Stoll, a. Savin and H. Preuss, *Theor. Chim. Acta*, 1989, **75**, 173–194.
- 46 M. Dolg, H. Stoll and H. Preuss, *Theor. Chim. Acta*, 1993, **85**, 441–450.
- 47 F. Neese, F. Wennmohs, A. Hansen and U. Becker, *Chem. Phys.*, 2009, **356**, 98–109.
- 48 S. Kossmann and F. Neese, *Chem. Phys. Lett.*, 2009, **481**, 240–243.
- 49 R. Izsák and F. Neese, *J. Chem. Phys.*, 2011, **135**, 144105.
- 50 F. Neese, *J. Comput. Chem.*, 2003, **24**, 1740–1747.
- 51 R. Kendall and H. A. Fruchtl, *Theor. Chem. Acc.*, 1997, **97**, 158–163.
- 52 K. Eichkorn, M. Htiser, R. Ahlrichs, K. Eichkorn, O. Treutler, H. Marco and R. Ahlrichs, *Chem. Phys. Lett.*, 1995, **240**, 283–290.
- 53 K. Eichkorn, F. Weigend, O. Treutler and R. Ahlrichs, *Theor. Chem. Acc.*, 1997, **97**, 119–124.
- 54 J. L. Whitten, *J. Chem. Phys.*, 1973, **58**, 4496–4501.
- 55 E. J. Baerends, D. E. Ellis and P. Ros, *Chem. Phys.*, 1973, **2**, 41–51.
- 56 B. I. Dunlap, J. W. D. Connolly and J. R. Sabin, *J. Chem. Phys.*, 1979, **71**, 3396–3402.
- 57 C. Van Alsenoy, *J. Comput. Chem.*, 1988, **9**, 620–626.
- 58 S. Grimme, J. Antony, S. Ehrlich and H. Krieg, *J. Chem. Phys.*, 2010, **132**, 154104.
- 59 E. R. Johnson, S. Keinan, P. Mori Sánchez, J. Contreras García, A. J. Cohen and W. Yang, *J. Am. Chem. Soc.*, 2010, **132**, 6498–6506.
- 60 R. Ditchfield, W. J. Hehre and J. A. Pople, *J. Chem. Phys.*, 1971, **54**, 724–728.
- 61 W. J. Hehre, R. Ditchfield and J. A. Pople, *J. Chem. Phys.*, 1972, **56**, 2257–2261.
- 62 P. C. Hariharan and J. A. Pople, *Theor. Chim. Acta*, 1973, **28**, 213–222.
- 63 S. Stoll and A. Schweiger, *J. Magn. Reson.*, 2006, **178**, 42–55.
- 64 R. A. Fields and C. A. Hutchison Jr., *J. Chem. Phys.*, 1985, **82**, 1711–1722.
- 65 G. Leniec, S. M. Kaczmarek, J. Typek, B. Kołodziej, E. Grech and W. Schilf, *J. Phys.: Condens. Matter*, 2006, **18**, 9871–9880.
- 66 A. Collauto, A. Feintuch, M. Qi, A. Godt, T. Meade and D. Goldfarb, *J. Magn. Reson.*, 2016, **263**, 156–163.
- 67 F. A. Cotton and G. Wilkindson, *Advanced Inorganic Chemistry*, Wiley, New York, 6th edn, 1999.
- 68 G. Johansson and H. Wakita, *Inorg. Chem.*, 1985, **24**, 3047–3052.
- 69 T. Shi, A. C. Hopkinson and K. W. M. Siu, *Chem. – Eur. J.*, 2007, **13**, 1142–1151.
- 70 Y. Polyhach, A. Godt, C. Bauer and G. Jeschke, *J. Magn. Reson.*, 2007, **185**, 118–129.
- 71 I. Tkach, S. Pornsuwan, C. Höbartner, F. Wachowius, S. T. Sigurdsson, T. Y. Baranova, U. Diederichsen, G. Sicoli and M. Bennati, *Phys. Chem. Chem. Phys.*, 2013, **15**, 3433–3437.
- 72 G. W. Reginsson, R. I. Hunter, P. a S. Cruickshank, D. R. Bolton, S. T. Sigurdsson, G. M. Smith and O. Schiemann, *J. Magn. Reson.*, 2012, **216**, 175–182.
- 73 A. Savitsky, A. Dubinskii, H. Zimmermann, W. Lubitz and K. Möbius, *J. Phys. Chem. B*, 2011, **115**, 11950–11963.
- 74 M. Gordon-Grossman, I. Kaminker, Y. Gofman, Y. Shai and D. Goldfarb, *Phys. Chem. Chem. Phys.*, 2011, **13**, 10771–10780.
- 75 D. Samanta, P. P. Borbat, B. Dzikovski, J. H. Freed and B. R. Crane, *Proc. Natl. Acad. Sci. U. S. A.*, 2015, **2**, 2455–2460.
- 76 A. Raitsimring, A. Dalaloyan, A. Collauto, A. Feintuch, T. Meade and D. Goldfarb, *J. Magn. Reson.*, 2014, **248**, 71–80.
- 77 L. Garbuio, K. Zimmermann, D. Häussinger and M. Yulikov, *J. Magn. Reson.*, 2015, **259**, 163–173.
- 78 I. Kaminker, I. Tkach, N. Manukovsky, T. Huber, H. Yagi, G. Otting, M. Bennati and D. Goldfarb, *J. Magn. Reson.*, 2013, **227**, 66–71.

- 79 A. Raitsimring, A. Astashkin, J. H. Enemark, A. Blank, Y. Twig, Y. Song and T. J. Meade, *Appl. Magn. Reson.*, 2012, **42**, 441–452.
- 80 C. T. Loh, K. Ozawa, K. L. Tuck, N. Barlow, T. Huber, G. Otting and B. Graham, *Bioconjugate Chem.*, 2013, **24**, 260–268.
- 81 S. Razzaghi, M. Qi, A. I. Nalepa, A. Godt, G. Jeschke, A. Savitsky and M. Yulikov, *J. Phys. Chem. Lett.*, 2014, **5**, 3970–3975.
- 82 A. Doll, M. Qi, N. Wili, S. Pribitzer, A. Godt and G. Jeschke, *J. Magn. Reson.*, 2015, **259**, 153–162.